Int. J. Therm. Sci. (2000) 39, 709–720

S1290-0729(00)00224-6/FLA

Turbulent fluid flow, heat transfer and onset of nucleate boiling in annular finned passages

Sang Y. Shim [a], Hassan M. Soliman [b]*, Grant E. Sims [b]

[a] *Atomic Energy Control Board, P.O. Box 1046, Ottawa, ON, K1P 5S9, Canada*

[b] *Department of Mechanical and Industrial Engineering, University of Manitoba, Winnipeg, MB, R3T 5V6, Canada*

(Received 23 September 1999, accepted 1 December 1999)

Abstract — An analytical model has been formulated for fully-developed turbulent flow and heat transfer in finned annuli using a modified mixing-length turbulence model. The model accounts for the conjugate heat transfer in the fluid and the solid, and the finite thickness of the fins. Solutions were obtained using the finite element method adopting a mesh that exactly fits the solution domain with fine elements near the solid boundaries. Predictions of the model have been compared with experimental results for smooth and finned annuli with generally good agreement between data and predictions. The model has been extended to predict the conditions at the onset of nucleate boiling using the criterion of Davis and Anderson. Again, these predictions agreed well in magnitude and trend with experimental data of finned annuli. © 2000 Éditions scientifiques et médicales Elsevier SAS

turbulent flow / conjugate heat transfer / finned annuli / onset of nucleate boiling

Nomenclature

C_p	specific heat	$J \cdot kg^{-1} \cdot K^{-1}$
D_f	van Driest damping function	
D_h	hydraulic diameter	m
h_{fg}	latent heat of vaporization	$J \cdot kg^{-1}$
k	thermal conductivity	$W \cdot m^{-1} \cdot K^{-1}$
L	Nikuradse-type mixing length	m
l	mixing length	m
$\dot{m}$	mass flow rate	$kg \cdot s^{-1}$
p	pressure	Pa
Pr	Prandtl number $= \mu C_p / k$	
Q_{gen}	rate of heat generation per unit volume	$W \cdot m^{-3}$
r	radial coordinate	m
r_i	inner radius of annulus	m
r_m	radius of maximum velocity	m
r_o	outer radius of annulus	m
Re	Reynolds number $= w_m D_h / \nu$	
s	circumferential distance (*figure 2*)	m
s_o	half distance between adjacent fins (*figure 2*)	m
T	temperature	K
W	input power to heater	W
w	velocity	$m \cdot s^{-1}$
w_m	mean velocity	$m \cdot s^{-1}$
y	coordinate measured normal to wall	m
z	axial coordinate	m

Greek symbols

θ	angular coordinate	
θ_o	half-angle between two adjacent fins	
μ	viscosity	$N \cdot s \cdot m^{-2}$
ν	kinematic viscosity	$m^2 \cdot s^{-1}$
ρ	density	$kg \cdot m^{-3}$
σ	surface tension	$N \cdot m^{-1}$
τ_w	wall shear stress	Pa

Subscripts

1, 2	regions 1 and 2 in *figure 1*
f	fluid
ft	fin tip
sat	saturation
sh	sheath midway between two adjacent fins
t	turbulent
v	vapor
w	wall

* Correspondence and reprints.
hsolima@cc.umanitoba.ca

1. INTRODUCTION

Fins are often used in the energy industry in order to enhance the heat transfer rate (e.g., compact heat exchangers, and nuclear fuel elements). Details of the fluid-flow and heat-transfer characteristics are necessary for the optimum design of finned passages for the given constraints of each particular application.

For smooth annuli, a large number of experimental and analytical studies (e.g., [1–15]) have been performed to investigate the characteristics of turbulent fluid flow and heat transfer. Some of these studies [2, 6, 7] have dealt with developing flow in the entrance region; however, most of the studies dealt with fully-developed flow. All referenced studies dealt with concentric annuli, except for [6] that considered eccentric annuli as well. Lee and Kim [9] studied the transverse curvature effects on the external flow along a cylindrical body that were relevant to the inner tube of an annulus. Air was used as the test fluid in most of the studies [1–12], while water was used in [13–15]. Typically, these studies covered a narrow range of Reynolds number.

In contrast to the geometry of smooth annuli, information on turbulent fluid flow and heat transfer in finned annuli is rather limited in the literature. Patankar et al. [16] presented an analytical model for fully developed turbulent air flow in internally finned tubes and annuli. Their model assumed zero-thickness fins, uniform wall temperature circumferentially in the tube wall and fins, and no secondary flow. Atomic Energy of Canada Limited (AECL) has performed experimental studies on the problem of finned annuli. The development of high-flux nuclear reactors requires the design of a nuclear fuel element that dissipates heat more effectively to the coolant. This was achieved by installing a number of longitudinal, rectangular fins on the thin sheath surrounding the fuel pin. An experimental test facility was constructed to study the pressure-drop and heat-transfer characteristics of these finned fuel pins under various operating conditions [17]. Experimental data were generated in the fully-developed region and the measurements included the sheath temperature midway between two adjacent fins, the fin-tip temperature, the pressure gradient, and the input power at the onset of nucleate boiling (ONB) [18, 19]. However, detailed flow and temperature measurements were not made in these studies.

It is evident from the above review that there is a need to develop a theoretical model for turbulent flow and heat transfer in finned annuli capable of handling real practical applications. The model should take into consideration the finite thickness of the fins and the temperature variation within the solid as well as the fluid. Therefore, the problem must be treated as a conjugate heat-transfer problem.

The objectives of the present investigation are:

(1) To develop an analytical model (governing momentum and energy equations, and an appropriate turbulence model for closure) for fully-developed turbulent flow and heat transfer in annular finned passages. The model should simulate real practical conditions such as conjugate heat transfer in the fluid and solid regions, variable fluid properties, and finite-thickness fins.

(2) To validate the model by comparing its predictions against experimental data for smooth and finned annuli.

(3) To extend the model in order to be able to predict the ONB in finned annuli and to compare these results against available experimental data.

2. MATHEMATICAL MODELLING

Figure 1 shows an internally finned annulus that will be used as the basic geometry for modelling in the present study. The cross-section consists of three regions: region 1 is the heater tube where a uniform rate of internal heat generation Q_{gen} is assumed, region 2 is the sheath and fins which is assumed to be in perfect contact with region 1, and region 3 is the fluid region. The inner surface of region 1 and the outer surface of region 3 are assumed to be adiabatic. Because of symmetry, computations will only be necessary over a section that spans half the space between two adjacent fins (section A-A in *figure 1*).

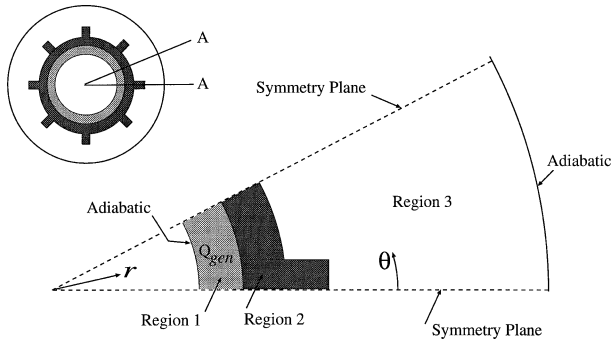

Figure 1. Geometry and coordinate system of the finned annulus used in modelling.

2.1. Governing equations and boundary conditions

The cylindrical coordinate system (r, θ, z) was used in the present study, where r and θ are the radial and angular coordinates (shown in *figure 1*), and z is the axial coordinate normal to the page. Steady, fully-developed flow (both hydrodynamically and thermally) of an incompressible fluid is assumed. Similar to [16], the secondary flow normal to the main axial flow is assumed to be negligible. Under these assumptions, the governing equations can be written as follows.

The energy equation for region 1 is given by

$$\frac{1}{r}\frac{\partial}{\partial r}\left(k_1 r \frac{\partial T}{\partial r}\right) + \frac{1}{r^2}\frac{\partial}{\partial \theta}\left(k_1 \frac{\partial T}{\partial \theta}\right) + Q_{\text{gen}} = 0 \quad (1)$$

The energy equation for region 2 is similar to that of region 1 except for the heat generation term, i.e.

$$\frac{1}{r}\frac{\partial}{\partial r}\left(k_2 r \frac{\partial T}{\partial r}\right) + \frac{1}{r^2}\frac{\partial}{\partial \theta}\left(k_2 \frac{\partial T}{\partial \theta}\right) = 0 \quad (2)$$

For the fluid flow in region 3, the momentum equation is given by

$$\frac{1}{r}\frac{\partial}{\partial r}\left[r(\mu_{\text{f}} + \mu_{\text{t}})\frac{\partial w}{\partial r}\right] + \frac{1}{r^2}\frac{\partial}{\partial \theta}\left[(\mu_{\text{f}} + \mu_{\text{t}})\frac{\partial w}{\partial \theta}\right] - \frac{\mathrm{d}p}{\mathrm{d}z} = 0 \quad (3)$$

where μ_{f} and μ_{t} are the molecular and turbulent viscosities, respectively, and the axial pressure gradient $\mathrm{d}p/\mathrm{d}z$ is treated as a constant due to the fully-developed-flow condition. The energy equation for region 3 can be written as

$$\frac{1}{r}\frac{\partial}{\partial r}\left[r(k_{\text{f}} + k_{\text{t}})\frac{\partial T}{\partial r}\right] + \frac{1}{r^2}\frac{\partial}{\partial \theta}\left[(k_{\text{f}} + k_{\text{t}})\frac{\partial T}{\partial \theta}\right] - \rho_{\text{f}} C_{p_{\text{f}}} w \frac{\mathrm{d}T}{\mathrm{d}z} = 0 \quad (4)$$

where k_{f} and k_{t} are the molecular and turbulent thermal conductivities for region 3, respectively, and $\mathrm{d}T/\mathrm{d}z$ is the axial temperature gradient, which is treated as a constant due to the fully-developed condition and the uniform rate of heat generation in region 1.

In equations (1)–(4), $k_1, k_2, k_{\text{f}}, \rho_{\text{f}}, C_{p_{\text{f}}}, \mu_{\text{f}}$, and Q_{gen} are known quantities. Models need to be formulated for μ_{t} and k_{t}. The value of $\mathrm{d}p/\mathrm{d}z$ can be determined from the fluid flow rate and $\mathrm{d}T/\mathrm{d}z$ can be determined from

$$\frac{\mathrm{d}T}{\mathrm{d}z} = \frac{Q_{\text{gen}} A_1}{\dot{m}_{\text{f}} C_{p_{\text{f}}}} \quad (5)$$

where A_1 is the cross-sectional area of region 1. The necessary boundary conditions are as follows:

(1) $\partial w/\partial\theta = \partial T/\partial\theta = 0$ at the symmetry planes of all three regions,

(2) $\partial T/\partial r = 0$ at the inner surface of region 1 and the outer surface of region 3,

(3) continuity of temperature and heat flux at the interface between regions 1 and 2, and the interface between regions 2 and 3,

(4) a reference temperature is specified at any arbitrary point in region 3,

(5) $w = 0$ at all walls.

2.2. Turbulence model

Although considerable effort has been devoted to the development and evaluation of different turbulence models, to date no model has been found to be both accurate and general for all flow geometries. A number of candidate turbulence models were reviewed [20] and the mixing-length model (also called the zero-equation model) was chosen for the present study. This model was also used in the analysis reported by Patankar et al. [16]; however, there are some key differences between the present application of the mixing-length model and the one in [16], which will be pointed out later.

The turbulence model is needed for the evaluation of μ_{t} and k_{t}, which appear in equations (3) and (4). Using the mixing-length model, a commonly used formulation for μ_{t} is given by

$$\mu_{\text{t}} = \rho_{\text{f}} l^2 \left[\left(\frac{\partial w}{\partial r}\right)^2 + \left(\frac{1}{r}\frac{\partial w}{\partial \theta}\right)^2\right]^{1/2} \quad (6)$$

where l is the mixing length. The tube wall and the fin surface simultaneously influence the value of l. The closer a point to one of these surfaces, the greater should be the effect of that surface on the resultant value of l. To fulfill this requirement, a superposition method (proposed in [16]) is used

$$\frac{1}{l} = \frac{1}{l_{\text{p}}} + \frac{1}{l_{\text{c}}} \quad (7)$$

where l_{p} is the mixing length for pipe flow (without fins) and l_{c} is the mixing length for parallel plate channels (which simulate the space between the fins). The l_{c} component was formulated based on Nikuradse's work on the mixing-length model (referred to in [21]) and van Driest [22] damping function D_{f}. Accordingly,

$$l_{\text{c}} = (D_{\text{f}})_{\text{c}} L_{\text{c}} \quad (8)$$

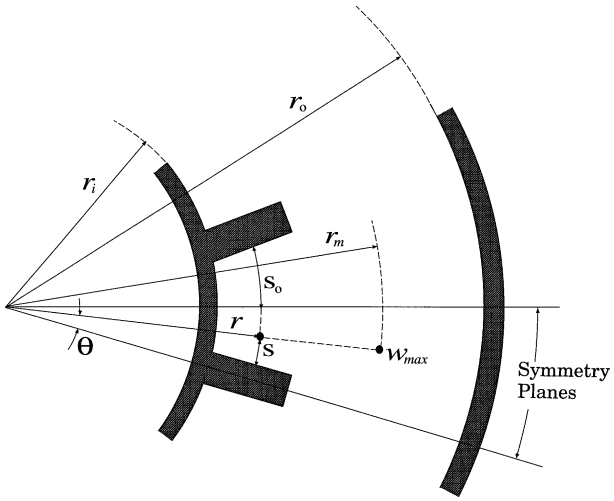

Figure 2. Definition of parameters used in the turbulence model.

where

$$(D_f)_c = 1 - \exp\left(-\frac{s^+}{A^+}\right) \tag{9}$$

and

$$\frac{L_c}{s_o} = 0.8 - 1.4\left(1 - \frac{s}{s_o}\right)^2 + 0.6\left(1 - \frac{s}{s_o}\right)^4 \tag{10}$$

As shown in *figure 2*, s_o is half the arc length between two adjacent fins at a given radius r, and s is the arc length between a point (r, θ) and the fin surface. The dimensionless parameter s^+ is given by

$$s^+ = s\,\frac{\sqrt{\tau_w/\rho_f}}{\nu} \tag{11}$$

where τ_w is the local shear stress at the fin surface, and $A^+ = 26$.

In formulating the l_p component, consideration must be given to the form of the fully-developed velocity profile in a smooth annulus with inner radius r_i and outer radius r_o. The velocity is zero at $r = r_i$, increases to a maximum at $r = r_m$, and decreases again to zero at $r = r_o$. Therefore, if we are to use pipe-flow-type formulae for l_p, we must develop one equation for the inner region ($r_i \le r \le r_m$) and a different equation for the outer region ($r_m \le r \le r_o$).

Define

$$\begin{aligned} y &= r - r_i, & y_m &= r_m - r_i \\ y_o &= r_o - r_i, & y_{om} &= y_o - y_m \end{aligned} \tag{12}$$

Again, using a Nikuradse-type mixing-length model, we get

$$l_p = (D_f)_p L_p \tag{13}$$

where

$$(D_f)_p = 1 - \exp\left(-\frac{y^+}{A^+}\right) \tag{14}$$

$$y^+ = y\,\frac{\sqrt{\tau_w/\rho_f}}{\nu} \tag{15}$$

and $A^+ = 26$. In the inner region, τ_w is the local shear stress at $r = r_i$ and $L_p = L_i$. In the outer region, τ_w is the local shear stress at $r = r_o$ and $L_p = L_o$. Values of L_i and L_o can be determined from

$$\frac{L_i}{y_m} = b_1 - b_2\left(1 - \frac{y}{y_m}\right)^2 - b_3\left(1 - \frac{y}{y_m}\right)^4 \tag{16}$$

and

$$\frac{L_o}{y_{om}} = C_1 - C_2\,\frac{(y - y_m)^2}{y_{om}^2} - C_3\,\frac{(y - y_m)^4}{y_{om}^4} \tag{17}$$

The flow in the outer region is similar to pipe flow and, therefore, the constants in equation (17) can be taken as $C_1 = 0.14$, $C_2 = 0.08$, and $C_3 = 0.06$ (Nikuradse [21]). The coefficients in equation (16) must satisfy the following conditions:

$$\begin{aligned} &\text{(a)} \quad L_i = 0 && \text{at } y = 0 \\ &\text{(b)} \quad \frac{\partial L_i}{\partial y} = K_i && \text{at } y = 0, \quad \text{and} \\ &\text{(c)} \quad L_i = L_o && \text{at } y = y_m \end{aligned} \tag{18}$$

Applying conditions (18) to equation (16), we get:

$$\begin{aligned} b_1 &= 0.14\frac{y_{om}}{y_m} \\ b_2 &= 2b_1 - 0.5K_i, \quad \text{and} \\ b_3 &= 0.5K_i - b_1 \end{aligned} \tag{19}$$

The value of K_i was determined from the following relationship derived by Roberts [3]:

$$\frac{K_i}{K} = \frac{r_o - r_m}{r_m - r_i}\left[\frac{r_i(r_o^2 - r_m^2)}{r_o(r_m^2 - r_i^2)}\right]^{1/2} \tag{20}$$

where K is the von Karman constant ($K = 0.4$).

Similarly, the mixing length influenced by the fin tip and the outer wall was obtained using the same procedure described above. The only difference is that the distance

from the inner wall was replaced by the distance from the fin tip.

Equations (6)–(20) provide a complete model for the determination of μ_t subject to knowledge of r_m. For smooth annuli, the value of r_m is independent of θ, while for finned annuli, r_m can vary significantly with θ. In both cases, the location of the maximum velocity in each radial line was determined numerically during the iterative solution procedure.

The turbulent thermal conductivity k_t was determined from the well-known relation

$$k_t = k_f \frac{\mu_t}{\mu_f} \frac{Pr_f}{Pr_t} \tag{21}$$

where Pr_t is the turbulent Prandtl number, which was given a value of 0.9 throughout this investigation.

In the case of smooth annuli, the mixing-length theory has an inherent shortcoming that μ_t, as defined by equation (6), becomes zero at the location of maximum velocity and thus, k_t becomes zero at this location, as predicted by equation (21). These values are physically incorrect according to the experimental measurements of Lee and Park [7] and Reichardt [23]. A correction is necessary; otherwise, the temperature profile near the location of maximum velocity will contain an unphysical kink. To remedy this shortcoming, the Reichardt [23] expression for μ_t was utilized. At $r = r_m$, the Reichardt expression reduces to

$$\mu_t = \rho_f \frac{K}{6}(r_o - r_m)\sqrt{\frac{\tau_w}{\rho_f}} \tag{22}$$

where K $(= 0.4)$ is the von Karman constant, and τ_w is the local shear stress at the outer wall of the annulus. The value of μ_t given by equation (22) was regarded as the minimum value that μ_t can assume in the neighbourhood of $r = r_m$.

Many features of the above turbulence model are similar to the model used by Patankar et al. [16]. However, two main differences exist between the two models. These differences are:

(1) The value of r_m was determined numerically in the present analysis (one r_m value along each radial line). Patankar et al. [16] used a correlation developed by Kays and Leung [1] which gave a single value for r_m over the whole computational domain. This difference influenced variables such as K_i in equation (20), the coefficients defined in equation (19), L_i in equation (16), and the shear stresses throughout the solution domain.

(2) The present analysis uses equation (22) for μ_t near the location of maximum velocity, while the analysis by Patankar et al. [16] allows μ_t to go to zero at this location.

3. NUMERICAL SOLUTION METHOD

The finite-element method was chosen as the solution method in the present study because of its ability to fit accurately an irregular geometry that contains curved and square boundaries such as a finned annulus. A variational approach [24] was used in obtaining the finite-element formulation of governing equations (1)–(4) with the specified boundary conditions. The variational formulation results in an integral form of each governing equation. The integral form was solved numerically for each element by transforming the physical coordinates of an element to the master coordinates through the Jacobian matrix. The element-based equations were combined with the adjacent elements by imposing continuity at the interfaces. When this algebraic equation was derived for all elements, it resulted in a matrix of algebraic equations for each of the dependent variables w and T. The matrix for each variable was then solved using a direct matrix solver. The procedure used in this study for generating the finite-element formulation, coordinate transformation, numerical integration, and assembling the matrix for each dependent variable is described in [20].

Accuracy of the solution depends largely on the mesh and nodal distribution over the solution domain. The present study followed these guidelines for mesh generation [24]:

(1) The mesh must accurately match the flow and solid boundaries of the computational domain.

(2) The regions of large gradients of w and/or T need to be represented by small elements or a fine grid.

(3) The mesh should not contain elements with very large aspect ratios or large angular distortions, especially in the regions of large gradients.

A mesh generation program was developed and used in the present investigation taking the above guidelines into consideration. A gradient option was used to allow the gradual stretching or clustering of the nodes, particularly near the wall boundaries. A structured scheme was used for ease of numbering and positioning of the elements and nodes.

An iterative procedure was followed in obtaining a solution of the governing equations. The discretized forms of the equations were solved sequentially using the most recent values of the fields when solving each equation. A relaxation factor of 0.5 was used in all the equations to

avoid numerical divergence. The solution for the laminar case was used as an initial guess of the fields. Iteration continued until the following convergence criterion was met:

$$\frac{\sum_{i=1}^{N} |\phi_i^n - \phi_i^{n-1}|}{N} \leq 5{\cdot}10^{-3} \qquad (23)$$

where ϕ is a dummy variable representing w in $\mathrm{m{\cdot}s^{-1}}$ or T in K, ϕ_i^n is the current value at node i, ϕ_i^{n-1} is the previous value at node i, and N is the total number of nodes. The use of criterion (23) resulted in maximum relative residuals (i.e. $|\phi_i^n - \phi_i^{n-1}|/\phi_i^n$) at all nodes that were less than $4{\cdot}10^{-6}$ for w and $3{\cdot}10^{-4}$ for T.

The converged solution was also tested to insure that it satisfied the overall momentum and energy balances. This was done by comparing the force due to the axial pressure gradient and the force due to wall friction and allowing less than 0.1% difference between the two forces. As well, the total rate of heat leaving the solid boundaries was compared with the total rate of heat gained by the fluid (region 3 in *figure 1*) and allowing a difference of less than 0.1 %. Further mesh refinements were made (particularly near the solid boundaries) when either of these conditions was not met.

Mesh-independence tests were conducted for each solution geometry. A description of the mesh used in generating the results for each geometry is given in the section where the results for that particular geometry are presented.

4. RESULTS AND DISCUSSION

The objectives of this section are: (a) to demonstrate the accuracy of the mathematical model and the finite-element numerical procedure, and (b) to establish the validity of the turbulence model to the geometries under consideration. These objectives were met by comparing the theoretical predictions of the present model with experimental data of smooth and finned annuli. Further, the model was extended in order to include the predictions of the Onset of Nucleate Boiling (ONB) in finned annuli and these predictions were validated with experimental data.

4.1. Smooth annuli

Fully-developed turbulent flow in smooth concentric annuli was predicted for a wide range of radius ratio r_o/r_i (1.6 to 80.7), Reynolds number Re_f (10^4 to 10^6), and Prandtl number Pr_f (0.7 to 10). A sample of the results is presented here and more results can be found in [20]. For this geometry, the boundary conditions reduce to uniform temperature and heat flux at $r = r_i$, adiabatic conditions at $r = r_o$, and axial symmetry (i.e. no variation in the θ direction).

Grid-independence tests were conducted [20] and it was found that good accuracy can be achieved with a grid that had 69 quadrilateral elements and 140 nodes. Due to axial symmetry, the grid was established over one stripe of the annulus with a width of 0.27°. The grid consisted of 10 elements close to the inner wall, 10 elements close to the outer wall, and 49 elements in the core joining the inner and outer regions. The appropriate size of the near-wall elements was found to decrease as Pr_f increased. The width of the angular stripe (0.27°), which determined the element aspect ratio, was chosen in accordance with the radial grid size.

Figure 3 shows a comparison between the predicted values of μ_t and the experimental data of Lee and Park [7] for $r_o/r_i = 2.31$ and $2.3{\cdot}10^4 \leq Re_f \leq 1.1{\cdot}10^5$. The present predictions and the measured profiles agree quite well for all values of Re_f. Both the model and the

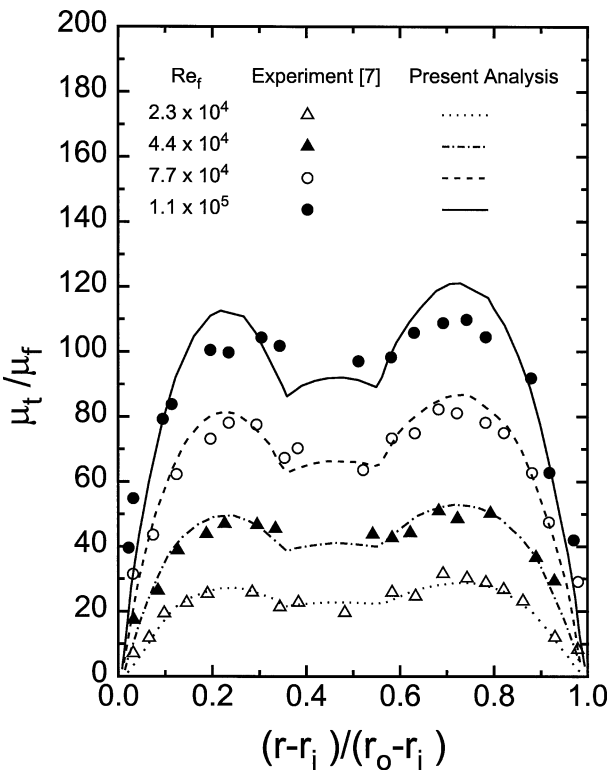

Figure 3. Comparison between data and predictions of turbulent viscosity for a smooth annulus with $r_o/r_i = 2.31$.

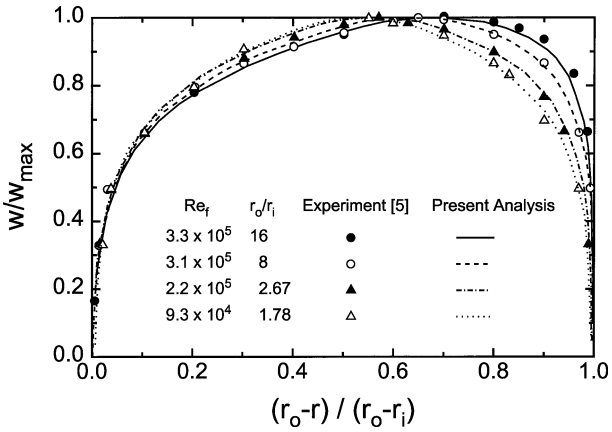

Figure 4. Comparison between data of Brighton and Jones [5] and present predictions of the velocity profiles in smooth annuli.

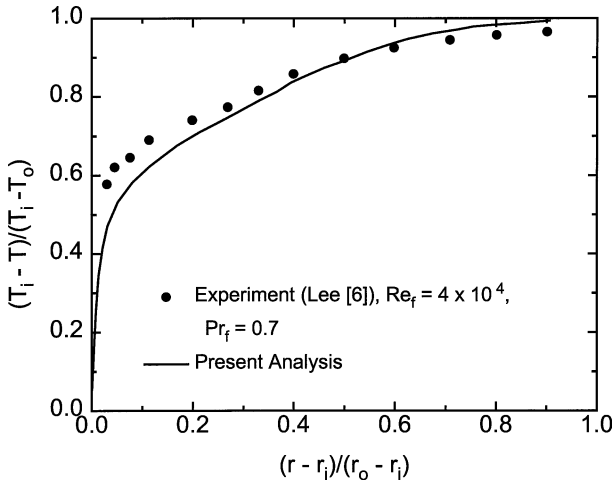

Figure 5. Comparison between data and predictions of the temperature profile in a smooth annulus with $r_o/r_i = 1.632$.

experimental results indicate that μ_t increases to a peak on both sides of the radius of maximum velocity and then decreases near the radius of maximum velocity, but does not go to zero. The classical mixing-length model will predict $\mu_t = 0$ at $r = r_m$; however, the present model avoids this situation by assuming a minimum value of μ_t near $r = r_m$ given by equation (22).

Predictions of the fully-developed velocity profiles are compared with the measurements of Brighton and Jones [5] in *figure 4* for $1.78 \leq r_o/r_i \leq 16$ and $9.3{\cdot}10^4 \leq Re_f \leq 3.3{\cdot}10^5$. Good agreement can be seen both inside and outside r_m for the whole range of test conditions. The value of r_m appears to be well predicted in all cases. As r_o/r_i increases, the value of r_m decreases which resulted in steeper velocity gradients near the inner wall.

Figure 5 shows a comparison between the predicted temperature profile and the experimental data of Lee [6] for $r_o/r_i = 1.632$, $Re_f = 4{\cdot}10^4$, and $Pr_f = 0.7$ (air). The data in *figure 5* correspond to $(T_i - T_o) = 29.2$ K and the maximum difference between the measured and calculated temperatures is about 3 K. The value of Nusselt number corresponding to the conditions in *figure 5* was calculated and found to be 5 % lower than the experimental value reported in [6].

4.2. Finned annuli

In this section, we examine the validity of the present model by comparing its predictions against experimental data generated at AECL for finned annuli [17–19]. Those experiments were conducted using a vertical test section that consisted of a finned pin placed inside a glass tube,

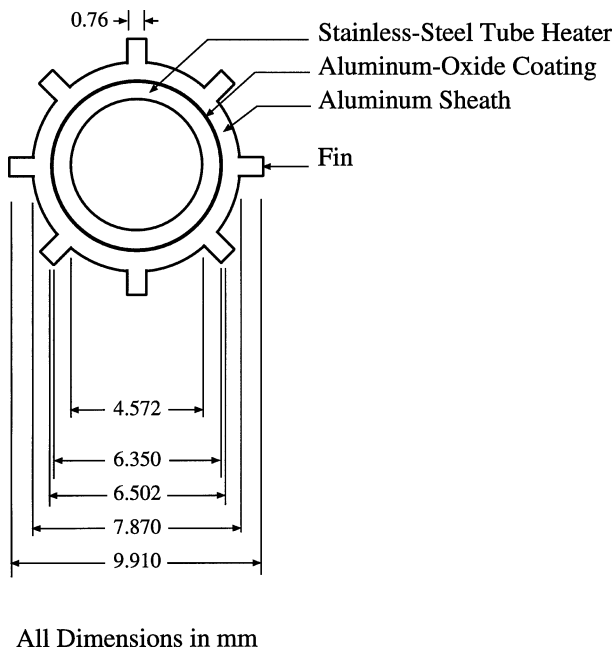

Figure 6. The finned-pin geometry used in [18].

thus forming a finned annulus. The finned pin, shown in *figure 6*, was constructed from a stainless-steel tube heater that was spray coated on the outside with a uniform layer of aluminum oxide (0.076 mm thick) for electrical insulation. An aluminum sheath with 8 longitudinal rectangular fins was used for cladding. The dimensions of the finned-pin geometry are shown in *figure 6*. Heat was generated at a uniform rate by passing electric currents through the tube heater. The glass tube surrounding the

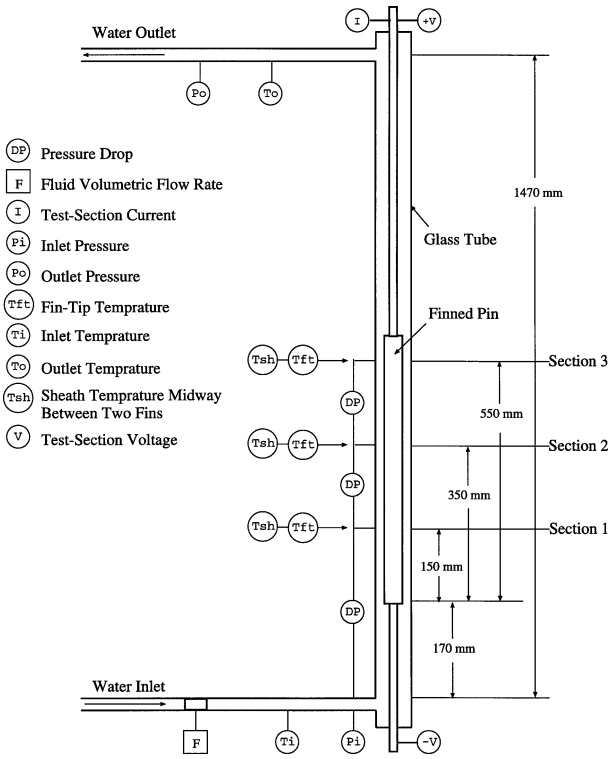

Figure 7. A schematic diagram of the test section and associated instrumentation used in [18].

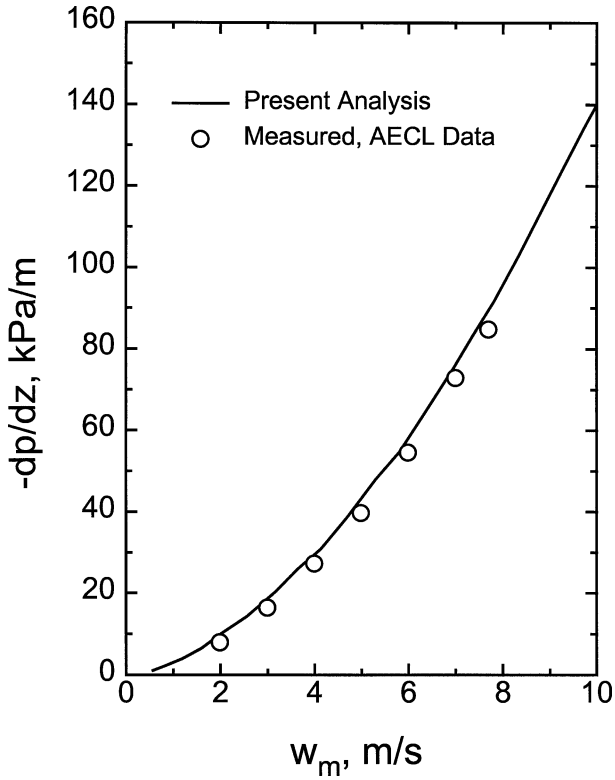

Figure 8. Comparison between the present predictions of the pressure gradient and AECL data for finned annuli.

finned pin had an inside diameter of 17 mm and thus, the hydraulic diameter was $D_h = 7.3$ mm. Adiabatic conditions are assumed at the inner surface of the heater tube and the outer glass tube.

A detailed schematic diagram of the test section and the associated instrumentation is shown in *figure 7*. Water was fed at the bottom of the test section and it flowed vertically upward towards the exit. The sheath (midway between two adjacent fins) and fin-tip (midpoint of the tip) temperatures were measured at three axial locations using type-K thermocouples. Water bulk temperatures were measured at the inlet and outlet of the test section using resistance thermometers. The pressure drops were measured between different locations in the test section, as shown in *figure 7*, using differential pressure transducers. The test-section inlet and outlet pressures were measured using absolute pressure transducers. A turbine meter was used to measure the volumetric flow rate of water at the test-section inlet. The power input was calculated from the voltage and current measured across the tube heater. Detailed information on the instrument calibration, test procedure, and estimates of experimental uncertainty can be found in [18–20].

Comparisons are made here against the data measured at section 3 in *figure 7*. This section was located 550 mm downstream from the inlet of the finned annulus (i.e. more than 75 hydraulic diameters) and, therefore, fully-developed conditions are assumed at this section. At this section, the bulk temperature was calculated from an energy balance using the inlet bulk temperature and the power input, and the value of the mean velocity was calculated from the measured volumetric flow rate at the test-section inlet.

The geometry under consideration here is similar to the one shown in *figure 1* with regions 1–3 representing the tube heater, the sheath and fins, and the fluid flow regions, respectively. Considering the symmetry of geometry, a one-sixteenth part of the cross-section in *figure 6* was discretized into a grid of 1 440 finite elements and 1 519 nodes. The grid covers the three regions (i.e. solving as a conjugate heat transfer problem) with 10 elements of fine size near all the solid boundaries.

Results of the pressure gradient $\mathrm{d}p/\mathrm{d}z$ at various mean velocities w_m are shown in *figure 8*. The experimental data in this figure were collected under isothermal conditions and the experimental uncertainty in $\mathrm{d}p/\mathrm{d}z$ was

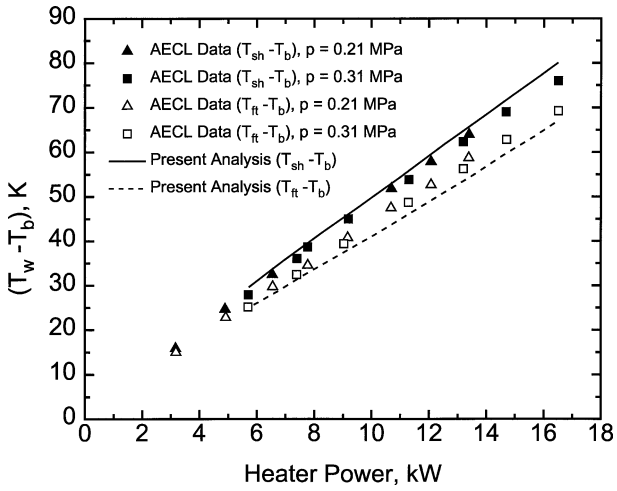

Figure 9. Comparison between the present predictions of the wall-to-bulk temperature difference and AECL data for finned annuli at $w_m = 1.2$ m·s^{-1}.

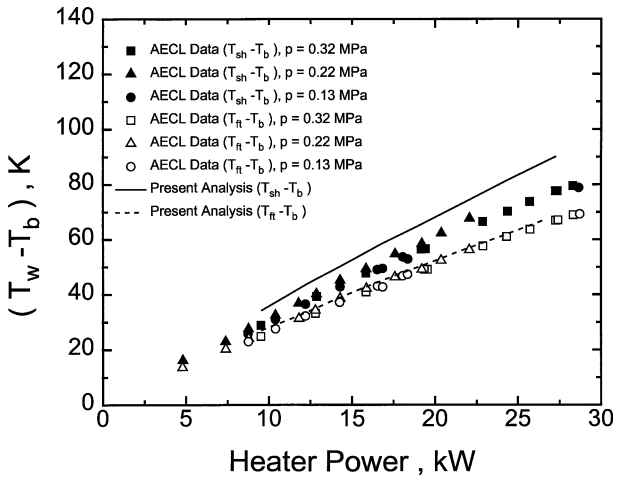

Figure 10. Comparison between the present predictions of the wall-to-bulk temperature difference and AECL data for finned annuli at $w_m = 2.0$ m·s^{-1}.

claimed to be within ± 0.45 kPa·m^{-1} [18]. Excellent agreement can be seen between the experimental data and the present model. The results exhibit the expected behaviour of increasing pressure gradient with increasing mean velocity.

Figures 9 and *10* show the variation of the sheath temperature T_{sh} and the fin-tip temperature T_{ft} with the input power W at the two mean velocities of 1.2 and 2.0 m·s^{-1}, respectively. The experimental data correspond to three pressures of approximately 0.13, 0.22, and 0.32 MPa. It can be seen from *figures 9* and *10* that the pressure has insignificant effect on the measured values of T_{sh} and T_{ft}, which is consistent with the present model. Both the data and the model show that T_{sh} is higher than T_{ft} and that the difference ($T_{sh} - T_{ft}$) increases as W increases. This variation in wall temperature confirms that the heat transfer in the solid (regions 1 and 2) is two-dimensional and, therefore, the problem must be solved as a conjugate problem, as was done in the present model. In both figures, the present model overestimates the ($T_{sh} - T_{ft}$) temperature difference. However, the agreement between data and model in both comparisons can certainly be considered reasonable when the experimental uncertainty is taken into consideration. According to Hembroff et al. [18], the measurement error of the wall temperature was ± 2 K and the experimental error in the bulk temperature was ± 1.2 K. Therefore, the experimental data of wall-to-bulk temperature difference in *figures 9* and *10* are within ± 2.3 K.

The experimental studies reported in [17–19] did not include detailed measurements of the velocity and temperature profiles in the flow domain. However, data were reported on the ONB and, therefore, the present model was extended to include the prediction of the phenomenon, as described in the following section.

4.3. Onset of nucleate boiling

4.3.1. Background

Figures 9 and *10* show that T_{sh}, which is the highest temperature in the cross-section, increases continuously with W. At high enough values of W, T_{sh} reaches a level whereby boiling can be initiated. The onset of nucleate boiling (ONB) is defined as the condition at which the first vapor bubble appears on the heating surface. Several ideas and modelling approaches have been suggested for determining the conditions at ONB (e.g., [25–28]). Among these studies, the work of Davis and Anderson [28] was found to be the most applicable to the present investigation.

The model proposed by Davis and Anderson [28] is based on the thermodynamic equilibrium criterion (given by the Clausius–Clapeyron equation) and the Gibbs equation for the pressure difference across a curved surface. These two equations were combined to give the superheat equation for the ONB. They further proposed that if a sufficiently wide range of cavity sizes is present on the heating surface, the first cavities to become active will be those corresponding to equal slopes of the superheat equation and the temperature profile at the wall. For applications involving liquids with low

surface tension, Davis and Anderson developed a simple formulation for the heat flux at ONB given by

$$q = \frac{k_f h_{fg} \rho_v}{8\sigma T_{sat}} (T_w - T_{sat})^2 \qquad (24)$$

4.3.2. Application to finned annuli

Considering the finned annulus, shown in *figure 1*, and the corresponding model given by equations (1)–(4), it is possible to use this model in conjunction with equation (24) for predicting the conditions at ONB. The approach used in the present study is illustrated in *figure 11*. Using the heat flux q and the temperature difference $(T_w - T_{sat})$ as coordinates, equation (24) can be plotted, as shown in *figure 11*. The saturation temperature T_{sat} corresponds to the local pressure at the cross-section for which the ONB is to be predicted, and all properties (k_f, h_{fg}, ρ_v, and σ) were calculated at T_{sat}. Consequently, the position of the line representing equation (24) in *figure 11* is a function of pressure. As well, the present model can be executed for fixed mean velocity and subcooling with various rates of heat generation Q_{gen} and produce a plot of q (the local heat flux midway between two adjacent fins) and $(T_w - T_{sat})$, where $T_w = T_{sh}$. The position of this line would depend on the mean velocity and subcooling. The conditions at ONB (heat flux and local superheat) were assumed to be those corresponding to the point of intersection in *figure 11*. These conditions at ONB are therefore dependent on pressure, mean velocity, and subcooling.

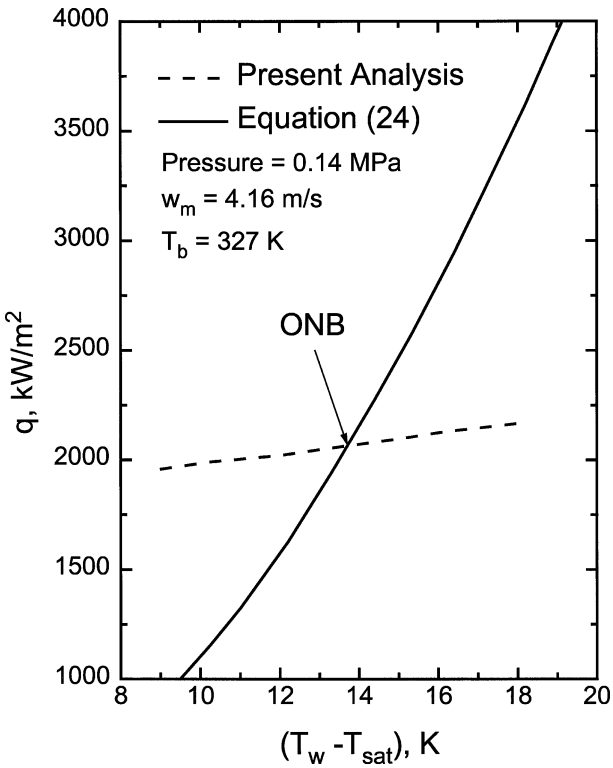

Figure 11. Graphical prediction of the conditions at ONB using the criterion of Davis and Anderson [28].

4.3.3. Comparison with experimental data

The AECL test facility, described briefly in Section 4.2 and *figures 6* and *7*, was also used for generating ONB data [17–19]. For various combinations of pressure, inlet temperature, and inlet flow rates, experiments were conducted at increasing finned-pin input power until ONB was detected at section 3 in *figure 7*. Values of W and T_{sh} at ONB were recorded in each experiment. The first appearance of vapor bubbles was detected visually with the aid of a stroboscopic light and an eight-power telescope. Dissolved and trapped noncondensable gases were removed from the test loop in each test. The first vapor bubbles were always observed on the sheath between the fins [18].

Comparisons were made between the AECL data and the present model following the procedure described in Section 4.3.2. The structure of the numerical grid used in these predictions was identical to the one used for the single-phase predictions. The predicted conditions at ONB correspond to the same values of mass flow rate, pressure, and bulk temperature reported in each experiment.

Figure 12 shows a comparison between the experimental and predicted values of W for two pressures (0.2

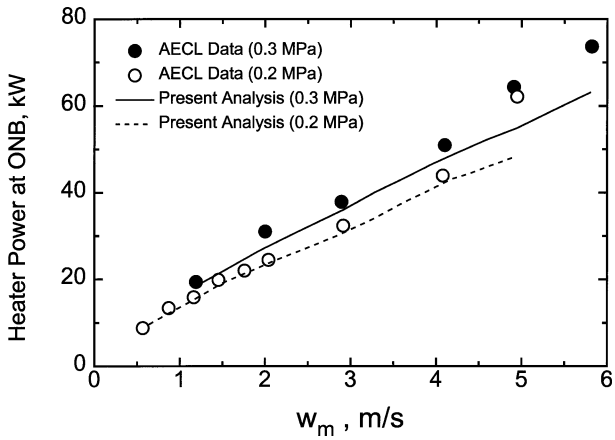

Figure 12. Comparison between the experimental and predicted values of W at ONB.

and 0.3 MPa) and a range of flow velocities. Excellent agreement can be seen up to $w_m = 4$ m·s^{-1}. For larger velocities, the experimental values of W appear to be significantly under-predicted by the model. As bubble size decreases with increasing flow rate, it is possible that visual observation may have missed the first appearance of bubbles, thus overestimating the value of W at ONB.

The effect of liquid subcooling (defined as the difference between saturation and bulk temperatures) on the value of W at ONB is shown in *figure 13*. Both data and predictions correspond to $p = 0.2$ MPa and $w_m = 1.15$ m·s^{-1}. *Figure 13* shows good agreement between data and predictions with a trend of increasing W at ONB with increasing liquid subcooling.

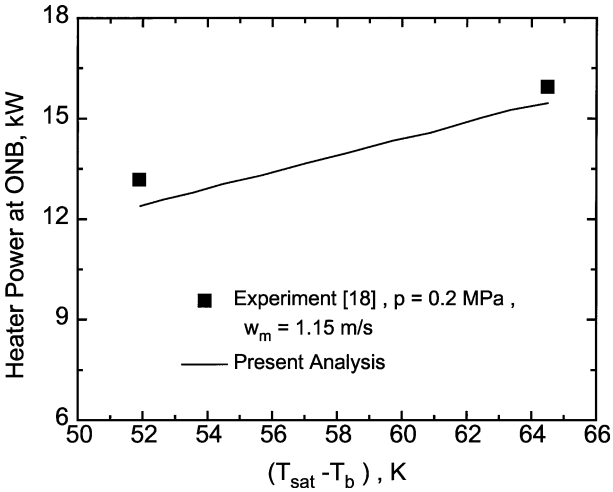

Figure 13. Effect of liquid subcooling on W at ONB.

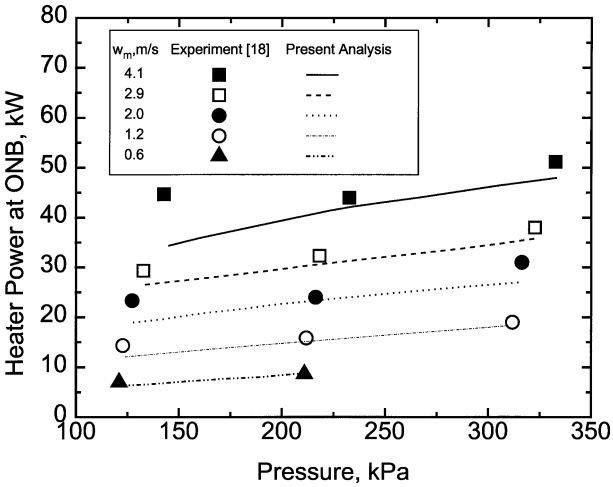

Figure 14. Effect of pressure on the value of W at ONB.

The effect of pressure on the value of W at ONB is illustrated in *figure 14*. The data correspond to a narrow range of bulk temperatures (54 °C $\leq T_b \leq$ 57 °C) but a wide range of mean velocities (0.6 m·s^{-1} $\leq w_m \leq$ 4.1 m·s^{-1}). Good agreement can be seen between data and predictions with a trend of increasing W at ONB with increasing p and/or w_m.

The root-mean-square deviation between the experimental and predicted values of W at ONB was calculated for all 25 data points and found to be approximately 13 %. This constitutes a satisfactory validation of the present modelling approach. The predicted ONB input powers were consistently lower than the measured ONB input powers.

5. CONCLUSIONS

A study was made of fully-developed turbulent flow and conjugate heat transfer in annular finned passages. The governing conservation equations of momentum and energy were formulated with a turbulence closure model based on the classical mixing-length theory. The mixing-length model was modified so that the value of the mixing length at a point can be determined by superimposing the contributions from its surrounding surfaces. The governing equations were solved using the finite-element method, thus producing detailed velocity and temperature distributions in finned annuli.

For the case of smooth annuli, fully-developed velocity and temperature profiles were predicted for wide ranges of r_o/r_i, Re_f, and Pr_f. The overall agreement between the present numerical results and data from different sources is quite good in terms of turbulent viscosity, velocity profile, and temperature profile.

The present model simulated AECL experiments on finned annuli and the results were compared with the measured pressure gradient and two local surface temperatures T_{sh} and T_{ft}. The predicted pressure gradient is in excellent agreement with the data and the predicted temperatures are in good agreement, particularly at low mean velocities. The predicted wall temperature peaked at the sheath centre between fins, and decreased along the fin side reaching a minimum at the centre of the fin tip.

The analysis was extended to predict the ONB for finned annuli using the criterion of Davis and Anderson [28]. The predicted ONB results showed good agreement with AECL data for finned annuli, particularly for $w_m < 4.0$ m·s^{-1}. Both the measured and predicted ONB occurred on the sheath centre. The predicted ONB fol-

lowed the trends in the data whereby W at ONB increased with w_m, p, and fluid subcooling.

Acknowledgements

The financial assistance provided by the Natural Sciences and Engineering Research Council of Canada is gratefully acknowledged. The authors would like to thank Dr. J.E. Kowalski, AECL Research, Whiteshell Laboratories for providing experimental data for the finned annulus geometry.

REFERENCES

[1] Kays W.M., Leung E.Y., Heat transfer in annular passages—hydrodynamically developed turbulent flow with arbitrarily prescribed heat flux, Int. J. Heat Mass Tran. 6 (1963) 537–557.

[2] Lee Y., Turbulent heat transfer from the core tube in thermal entrance regions of concentric annuli, Int. J. Heat Mass Tran. 10 (1967) 509–522.

[3] Roberts A., A comment on the turbulent flow velocity profile in a concentric annulus, Int. J. Heat Mass Tran. 10 (1967) 709–712.

[4] Barrow H., Lee Y., Roberts A., The similarity hypothesis applied to turbulent flow in an annulus, Int. J. Heat Mass Tran. 8 (1965) 1499–1505.

[5] Brighton J.A., Jones J.B., Fully developed turbulent flow in annuli, J. Basic Engineering 86 (1964) 835–844.

[6] Lee Y., Turbulent flow and heat transfer in concentric and eccentric annuli, Ph.D. Thesis, University of Liverpool, UK, 1964.

[7] Lee Y., Park S.D., Developing turbulent flow in concentric annuli: an analytical and experimental study, Wärme- und Stoffübertragung 4 (1971) 156–166.

[8] Shigechi T., Kawae N., Lee Y., Turbulent fluid flow and heat transfer in concentric annuli with moving core, Int. J. Heat Mass Tran. 33 (1990) 2029–2037.

[9] Lee Y., Kim K.C., An analysis on effect of transverse convex curvature on turbulent flow and heat transfer, Wärme- und Stoffübertragung 28 (1993) 89–95.

[10] Wilson N.W., Medwell J.O., An analysis of heat transfer for fully developed turbulent flow in concentric annuli, J. Heat Tran. 90 (1968) 43–50.

[11] Quarmby A., An analysis of turbulent flow in concentric annuli, Appl. Sci. Res. 19 (1968) 250–273.

[12] Rothfus R.R., Monrad C.C., Sikchi K.G., Heideger W.J., Isothermal skin friction in flow through annular sections, Ind. Engrg. Chem. 47 (1955) 913–918.

[13] Stein R.P., Begell W., Heat transfer to water in turbulent flow in internally heated annuli, AIChE J. 4 (1958) 127.

[14] Nixon M.L., Heat transfer to water flowing turbulently in tubes and annuli, AECL Internal Report, CRNL-165, 1968.

[15] Hasan A., Roy R.P., Kalra S.P., Velocity and temperature fields in turbulent liquid flow through a vertical concentric annular channel, Int. J. Heat Mass Tran. 35 (1992) 1455–1467.

[16] Patankar S.V., Ivanovic M., Sparrow E.M., Analysis of turbulent flow and heat transfer in internally finned tubes and annuli, J. Heat Tran. 101 (1979) 29–37.

[17] Spitz K.O., Kowalski J.E., Hembroff R.L., Baxter D.K., MAPLE heat transfer test facility, AECL Technical Note, MX10-03300-208-TN, 1989.

[18] Hembroff R.L., Kowalski J.E., Spitz K.O., McCallum C.K., Single-phase and boiling heat transfer measurements conducted in the MAPLE-X10 heat transfer test facility, AECL Technical Note, MX10-03300-233-TN, 1991.

[19] Hembroff R.L., Single-phase ΔP measurements and finned surface photographic study conducted in the single-pin heat transfer test facility, AECL Data Report, 1995.

[20] Shim S.Y., Turbulent fluid flow, heat transfer and onset of nucleate boiling in annular finned passages, Ph.D. Thesis, University of Manitoba, Canada, 1997.

[21] Schlichting H., Boundary Layer Theory, 7th Edition, McGraw-Hill, New York, 1979, p. 605.

[22] Van Driest E.R., On turbulent flow near a wall, J. Aero. Sci. 23 (1956) 1007–1011.

[23] Reichardt H., Vollständige Darstellung der turbulenten Geschwindigkeitsverteilung in glatten Leitungen, Zeitschrift für Angewandte Mathematik und Mechanik 31 (1951) 208–219.

[24] Reddy J.N., Gartling D.K., The Finite Element Method in Heat Transfer and Fluid Dynamics, CRC Press Inc., 1994.

[25] Hsu Y.Y., On the size range of active nucleation cavities on a heating surface, J. Heat Tran. 84 (1962) 207–216.

[26] Han C.Y., Griffith P., The mechanism of heat transfer in nucleate pool boiling—Part I: Bubble initiation, growth and departure, Int. J. Heat Mass Tran. 8 (1965) 887–904.

[27] Bergles A.E., Rohsenow W.M., The determination of forced-convection surface-boiling heat transfer, J. Heat Tran. 86 (1964) 365–372.

[28] Davis E.J., Anderson G.H., The incipience of nucleate boiling in forced convection flow, AIChE J. 12 (1966) 774–780.